catalysts

MDPI

Article

Photocatalytic Degradation of Estriol Using Iron-Doped TiO_2 under High and Low UV Irradiation

Irwing M. Ramírez-Sánchez [1] and Erick R. Bandala [2,3,*]

[1] Department of Civil, Architectural and Environmental Engineering, The University of Texas at Austin, Austin, TX 78712, USA; irwingmoises@gmail.com
[2] Desert Research Institute (DRI), 755 E. Flamingo Road, Las Vegas, NV 89119-7363, USA
[3] Graduate Program Hydrologic Sciences, University of Nevada, Reno, NV 89557, USA
* Correspondence: erick.bandala@dri.edu; Tel.: + 1-(702)-862-5395

Received: 29 September 2018; Accepted: 28 November 2018; Published: 5 December 2018

Abstract: Iron-doped TiO_2 nanoparticles (Fe-TiO_2) were synthesized and photocatalitically investigated under high and low fluence values of UV radiation. The Fe-TiO_2 physical characterization was performed using X-ray Powder Diffraction (XRD), Brunauer–Emmett–Teller (BET) surface area analysis, Transmission Electron Microscopy (TEM), Scanning Electron Microscopy (SEM), Diffuse Reflectance Spectroscopy (DRS), and X-ray Photoelectron Spectroscopy (XPS). The XPS evidenced that the ferric ion (Fe^{3+}) was in the TiO_2 lattice and unintentionally added co-dopants were also present because of the precursors of the synthetic method. The Fe^{3+} concentration played a key role in the photocatalytic generation of hydroxyl radicals ($^{\bullet}OH$) and estriol (E3) degradation. Fe-TiO_2 accomplished E3 degradation, and it was found that the catalyst with 0.3 at.% content of Fe (0.3 Fe-TiO_2) enhanced the photocatalytic activity under low UV irradiation compared with TiO_2 without intentionally added Fe (zero-iron TiO_2) and Aeroxide® TiO_2 P25. Furthermore, the enhanced photocatalytic activity of 0.3 Fe-TiO_2 under low UV irradiation may have applications when radiation intensity must be controlled, as in medical applications, or when strong UV absorbing species are present in water.

Keywords: iron-doped TiO_2; photocatalytic activity; low UV irradiation; hydroxyl radical; estriol

1. Introduction

In recent years, society and the scientific community have concerned of Emerging Contaminants (ECs, also called Contaminants of Emerging Concern), which are chemicals that threaten the environment, human health, and water safety and are not currently covered by existing local or international water quality regulations [1]. ECs include chemical species such as algae toxins, illegal drugs, industrial compounds, flame retardants, food additives, nanoparticles, pharmaceuticals (human and veterinary), personal care products, pesticides, biocides, steroids, synthetic and natural hormones, and surfactants [2].

Natural hormones (e.g., estrone (E1), 17β-estradiol (E2), and estriol (E3)) as ECs are susceptible of persisting and bioaccumulating in the environment, and could induce endocrine disruption in humans and wildlife (vertebrates [3–5] and invertebrates [6,7]). Natural attenuation, drinking water purification, and conventional municipal wastewater treatment processes are either incapable or only partially capable of removing estrogens from water [8]. As result, water treatment techniques are being developed to manage, reduce, degrade, and mineralize low-concentrated ECs (including natural estrogen) in drinking and wastewater [9]. Advanced Oxidation Processes (AOPs) are promising techniques to treat ECs in aqueous phase, which include well-known processes such as Fenton and Fenton-like processes, UV/H_2O_2, ozonation, and photocatalysis using semiconductors, peroxone

processes (H_2O_2/O_3), and cavitation [10,11]. Although there are many known AOPs, since Coleman's work [12], photocatalysis using titanium dioxide (TiO_2) has been identified as one of the most effective methods to degrade estrogens in water [13]. Several reports recognized that TiO_2 can degrade estrogens, which prevents increases in estrogenic activity in water [14,15] and partially or completely mineralizing estrogens [14,16].

Titanium dioxide is the most commonly used photocatalyst because of its reasonable optical and electronic properties, good photocatalytic activity, insolubility in water, chemical and photochemical stability, nontoxicity, low cost, and high efficiency in pollutant mineralization [17–20]. However, the band gap energy (E_g) of TiO_2, frequently reported as 3.2 eV [21], restrains the photocatalytic activation to energy sources with a portion of spectrum emission below 387.5 nm [22].

In general the photocatalytic mechanism is as shown in Figure 1. According to Density Functional Theory (DFT) computations, the valence band (VB) and conduction band (CB) of pure TiO_2 are mainly composed of O2p orbitals and Ti3d orbitals, respectively. Hence, the Fermi level (EF) is located in the middle of the band gap (BG), indicating that VB is full filled while CB is empty [23]. When using photons with energy higher than 3.2 eV, photoexcitation of the semiconductor promotes electrons from VB to CB creating a charge vacancy or hole (h^+) in the VB. The h^+ in the VB can react with hydroxide ion to form hydroxyl radical ($^\bullet$OH) or can also be filled by donor absorbed organic molecule (OM_{ads}). Photogenerated electrons in the CB can be transferred to acceptor of electrons and bring about $^\bullet$OH.

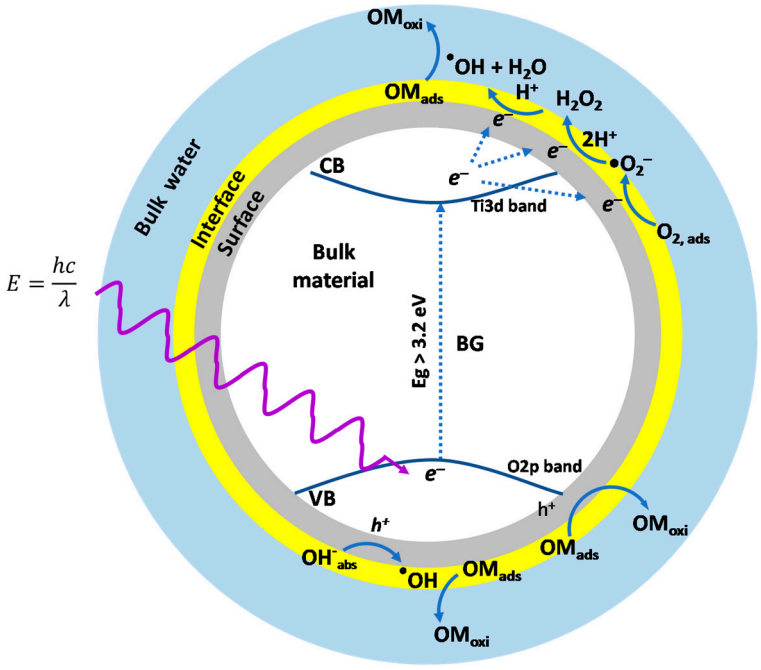

Figure 1. Photocatalytic mechanism of TiO_2 for $^\bullet$OH generation. Where E_g: Band gap energy; E: photon energy; OM_{ads}: adsorbed organic molecule; and OM_{oxi}: oxidized organic molecule.

Consequently, reducing the photon energy needed for TiO_2 photoactivation has been the focus of the scientific community until now. Doping is one of the techniques that has been tested to control or modify the surface properties or internal structure of TiO_2. Doping introduces a foreign element into TiO_2 to cause an impurity state in the band gap. The most frequently used doping materials are transition-metal cations (e.g., Cr, V, Fe, and Ni) at Ti sites, and anions (e.g., N, S, and C) at O sites [24]. Among anion- and cation-dopants, the ferric ion (Fe^{3+}) is one of the most often used because the ionic radius of Fe^{3+} (0.69 A) is similar to Ti^{4+} (0.745 A) [25]. Therefore, Fe^{3+} can be easily incorporated into the TiO_2 crystal lattice.

The main reported effects of iron-doped TiO_2 is a rapid increase in photocatalytic activity that increases with increased Fe doping, which then reaches a maximum value, and finally decreases with

further increased Fe content [23,26–37]. However, detrimental effects have been also reported because of high Fe content [38,39] or agglomerated Fe-TiO_2 nanoparticles [40,41].

Although several theoretical and experimental Fe-TiO_2 studies have been developed, the trade-off between doping ratio and radiation intensity is scarcely mentioned. Furthermore, Fe-TiO_2 photocatalyst has rarely been considered to be a useful technique for the degradation of E3 [42].

In this work, Fe-TiO_2 nanoparticles were synthesized to increase the understanding of the relationship between doping ratio and radiation intensity for hydroxyl radical (•OH) generation and E3 degradation. Therefore, we investigated the photocatalytic degradation of E3 using Fe-TiO_2 under high and low UV irradiation. We highlight the term low UV irradiation to avoid confusion with the term "photocatalytic processes under visible light" because we did not intentionally use UV cutoff filters for the experiments.

2. Results and Discussion

2.1. Characterization of Iron-Doped TiO_2

Figure 2 shows X-ray Photoelectron Spectroscopy (XPS) general spectra of TiO_2 without added Fe (zero-iron TiO_2) and Fe-TiO_2 materials (b, c, and d). For the experimental condition used, Fe did not affect the bonding structure between titanium and oxygen because the main peaks for all samples were Ti2p and O1s with the proportion 1:2.2, which is in agreement with the atomic formula of TiO_2.

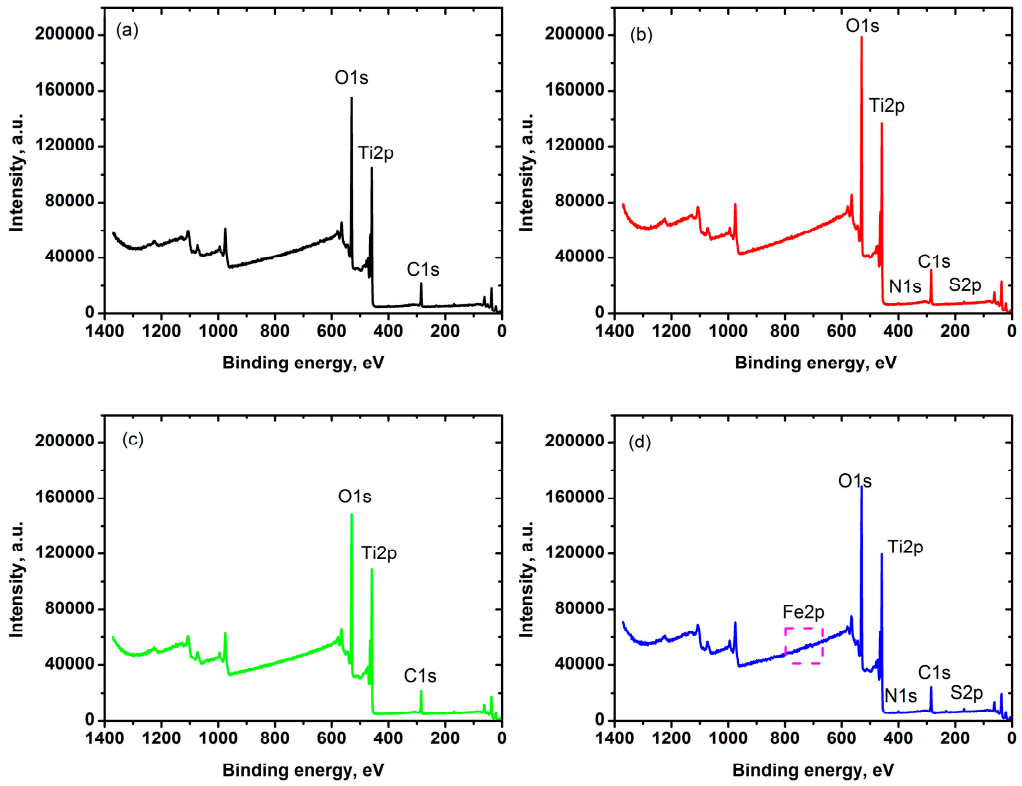

Figure 2. X-ray Photoelectron Spectroscopy (XPS) general spectra for zero-iron TiO_2 (**a**), 0.3 Fe-TiO_2 (**b**), 0.6 Fe-TiO_2 (**c**), and 1.0 Fe-TiO_2 (**d**).

XPS detected unintentionally added elements such as carbon, sulfur, and nitrogen (Table 1) as co-dopants of zero-iron TiO_2 and Fe-TiO_2, which were introduced into TiO_2 via precursors of the synthesis. Carbon and sulfur could come from sodium dodecyl sulfate (SDS), and nitrogen could come from iron (III) nitrate ($Fe(NO_3)_3 \cdot 9H_2O$) and HNO_3, all of them used in the synthesis process.

Table 1. Surface elemental composition determined by XPS.

Material	Atomic % of Elements (at.%)					
	Ti2p	O1s	C1s	Fe2p	S2p	N1s
Zero-iron TiO_2	24.4	52.9	21.3	0	1.4	-
0.3 Fe-TiO_2	23.8	51.1	22.9	0.3	1.1	0.8
0.6 Fe-TiO_2	23.9	53.1	22.5	0.6	-	-
1.0 Fe-TiO_2	23.5	52.5	20.6	1	1.5	0.9

High-resolution XPS spectra for the iron region (Figure 3) was studied only for 1.0 Fe-TiO_2 because no Fe2p signals were detected for zero-iron TiO_2, 0.3 Fe-TiO_2, or 0.6 Fe-TiO_2. The deconvolution of high-resolution XPS spectra (Figure 3) was developed for previously reported peaks of Fe^{2+} and Fe^{3+} [43]. Shirley baseline was subtracted before peak fitting. The Gaussian–Lorentzian mix function was used with a 40% factor. Charge compensation was set by the O1s peak charge with −0.58 eV. As a result, the correlation between the experimental signal and the theoretic model ($\Sigma\chi^2$) was 8.43×10^{-2}.

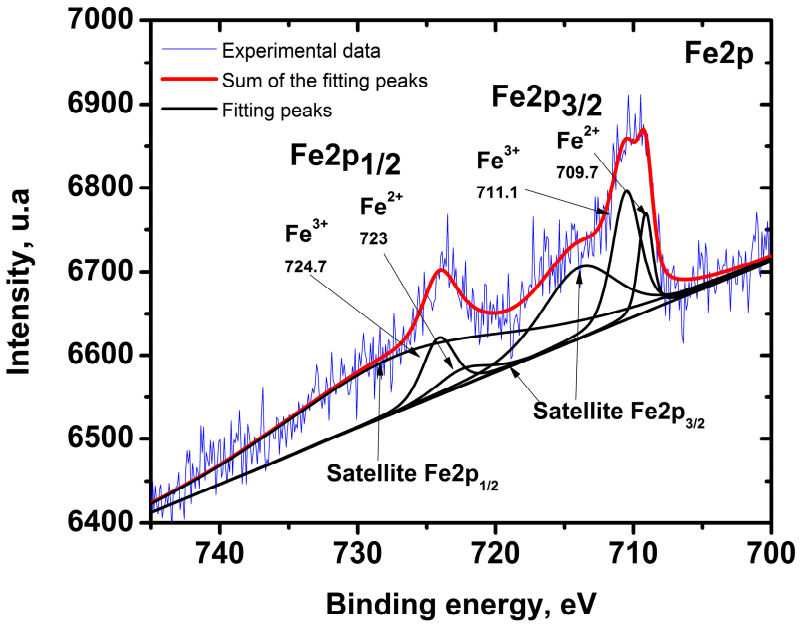

Figure 3. High-resolution XPS spectra for the iron region for 1.0 Fe-TiO_2.

According to the theoretical model (sum of fitting peaks), both Fe^{3+} and Fe^{2+} were present in the lattice of 1.0 Fe-TiO_2. We suggest that Fe^{3+} was incorporated into the lattice of TiO_2 to form Ti–O–Fe bonds, because the ionic radius of Fe^{3+} (0.69 A) is similar to the ionic radius of Ti^{4+} (0.745 A) [25]. The XPS technique detected Fe^{2+} because Fe^{3+} underwent reduction to Fe^{2+} during XPS measurement in vacuum [44].

The band gap energy (E_g) obtained with the Kubelka–Monk method (Figure 4) for Aeroxide® TiO_2 P25 was 3.2 eV, which is consistent with the value reported previously [45]. For Aeroxide® TiO_2 P25 E_g, red-shifts were detected as 0.22, 0.24, 0.25, and 0.3 eV for zero-iron TiO_2, 0.3 Fe-TiO_2, 0.6 Fe-TiO_2, and 1.0 Fe-TiO_2, respectively, which is consistent with values reported by Shi et al. of 0.25 eV [46] and with density functional theory calculations that suggested the hybridized band of Ti3d and Fe3d reduces E_g approximately 0.3–0.5 eV [44], or 0.2–0.34 eV [47].

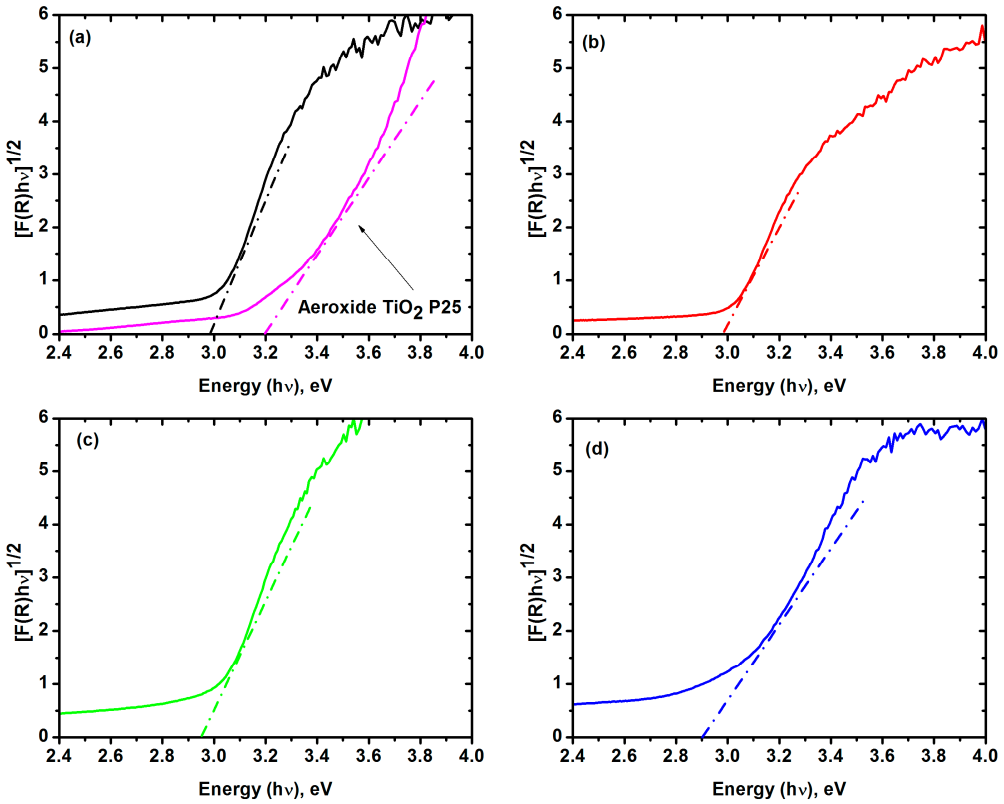

Figure 4. Band gap energy (E_g) by the Kubelka–Monk method. Zero-iron TiO_2 (**a**), 0.3 Fe-TiO_2 (**b**), 0.6 Fe-TiO_2 (**c**), and 1.0 Fe-TiO_2 (**d**).

For zero-iron TiO_2, E_g for Fe-TiO_2 materials (Table 2) decreased as long as the Fe content increased, so the Fe content generated red-shift. For Aeroxide® TiO_2 P25 E_g, the red-shift of Fe-TiO_2 agreed with previously reported values, but it agreed less for zero-iron TiO_2. Therefore, red-shift was not only related to Fe content, but also to the synthesis method and unintentionally co-doped TiO_2.

Table 2. Structural and optical properties of zero-iron TiO_2, and Fe-TiO_2.

Material	E_g		Anatase: Rutile	Particle Size	Surface Area	Pore Size	High UV	Low UV
	eV	nm	%	nm	$m^2\ g^{-1}$	nm	%	%
Aeroxide® TiO_2 P25	3.2 *	387.5 *	80:20 *	21 *	50 ± 15 *	17.5 *	36.4	0.8
Zero-iron TiO_2	2.98	416.1	73.1:26.9	6.6	66.5	8.4	99.26	7.64
0.3 Fe-TiO_2	2.96	418.9	77.9:21.1	6.9	77.6	1.2	99.40	8.21
0.6 Fe-TiO_2	2.95	420.3	78.8:21.2	7.1	73.0	1.4	99.42	8.77
1.0 Fe-TiO_2	2.90	427.6	76.3:23.7	6.9	83.1	9.4	99.43	10.63

* According to the manufacturer.

XRD patterns in Figure 5 revealed zero-iron TiO_2 and Fe-TiO_2 materials had both anatase and rutile phases. No XRD Fe_2O_3 peaks (2θ equal to 33.0°, 35.4°, 40.7°, 43.4°, and 49.2°) were observed, concluding that Fe^{3+} replaced Ti^{4+} in the TiO_2 crystal framework [48,49]. The synthesis method allowed uniform distribution of Fe within TiO_2. The anatase:rutile phase ratio calculated by Spurr and Myers' method showed that zero-iron TiO_2 and Fe-TiO_2 materials were a mixture of anatase and rutile phases (Table 2). The amount of anatase was less in Fe-TiO_2 materials than in Aeroxide® TiO_2 P25. The smaller proportion of anatase could lead to a reduction of photocatalytic activity because the anatase phase has higher photocatalytic activity than rutile TiO_2 [50,51]. However, it is accepted that the optimal photocatalytic activity of TiO_2 is reached with an optimal mixture of anatase and rutile phases [52]. Moreover, the increased anatase proportion in 0.3 Fe-TiO_2 and 0.6 Fe-TiO_2 compared

with zero-iron TiO_2 could improve photocatalytic activity. The increased anatase proportion was attributable to Fe doping disturbing the arrangements of TiO_2 phases [53]. This trend has also been observed when Fe-doped TiO_2 was synthesized using sol-gel [54] or co-precipitation methods [32].

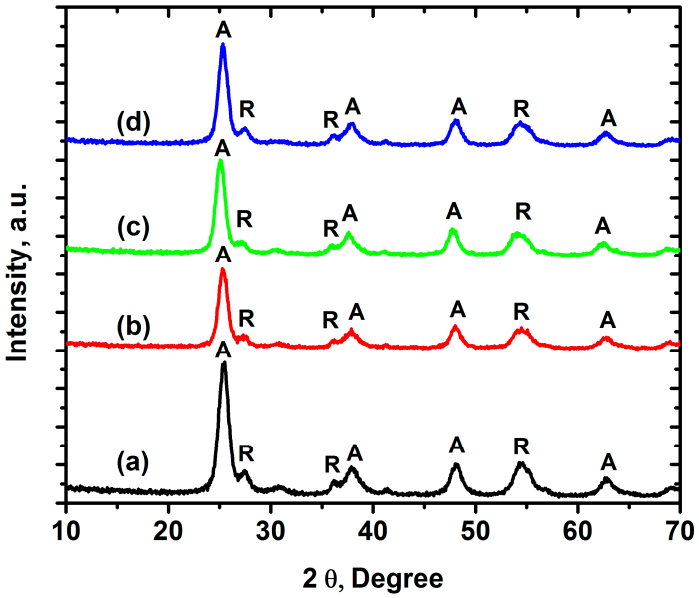

Figure 5. XRD patterns for zero-iron TiO_2 (**a**), 0.3 Fe-TiO_2 (**b**), 0.6 Fe-TiO_2 (**c**), and 1.0 Fe-TiO_2 (**d**), where A is Anatase and R is Rutile phases.

The average particle size of Fe-TiO_2 materials obtained by Scherrer's formula was 6.9 nm, which is less than the particle size of Aeroxide® TiO_2 P25 (Table 2). Fe-TiO_2 materials should increase photocatalytic activity because of their higher surface area and the short migration distance of the photogenerated charge carriers (electron/hole (e^-/h^+)) from the bulk material to the surface.

Further BET analysis (Figure 6) confirmed that average surface area of Fe-TiO_2 materials was 77.9 $m^2\ g^{-1}$, higher than zero-iron TiO_2 and Aeroxide® TiO_2 P25. BET isotherms followed a type IV shape according to the Langmuir classification, which is associated with the characteristics of mesoporous material [55]. The observed hysteresis is probably due to gas cooperative adsorption or condensation inside the pores of material [56]. BET analysis showed pore sizes (Table 2) were in the mesoporous range (2–50 nm, according to IUPAC classification) for zero-iron TiO_2 and 1.0 Fe-TiO_2, and the microporous range (0.2–2 nm, according to IUPAC classification) for 0.3 Fe-TiO_2 and 0.6 Fe-TiO_2. Mesoporous pore size should facilitate the mass transfer of reactants and products in the reaction system, so photocatalytic improvement based on this property could improve zero-iron TiO_2 and Fe-TiO_2 materials with respect to Aeroxide® TiO_2 P25 [31].

Patra et al. [49] developed a similar nanoparticle synthesis procedure, which generated surface area values ranging from 126 to 385 $m^2\ g^{-1}$ and mesoporous size distribution values ranging from 3.1 to 3.4 nm. Particles obtained in our work were different, probably because of the application of a mild thermal treatment and the use of SDS at critical micelle concentration as a template.

Figure 7 shows SEM images of agglomerated and assembled nanoparticles of zero-iron TiO_2. The different amounts of Fe in the TiO_2 lattice changed neither the particle size nor the morphology of the zero-iron TiO_2. Although the average pore size allowed an increase of the superficial area, agglomeration could lead to lower photocatalytic activity.

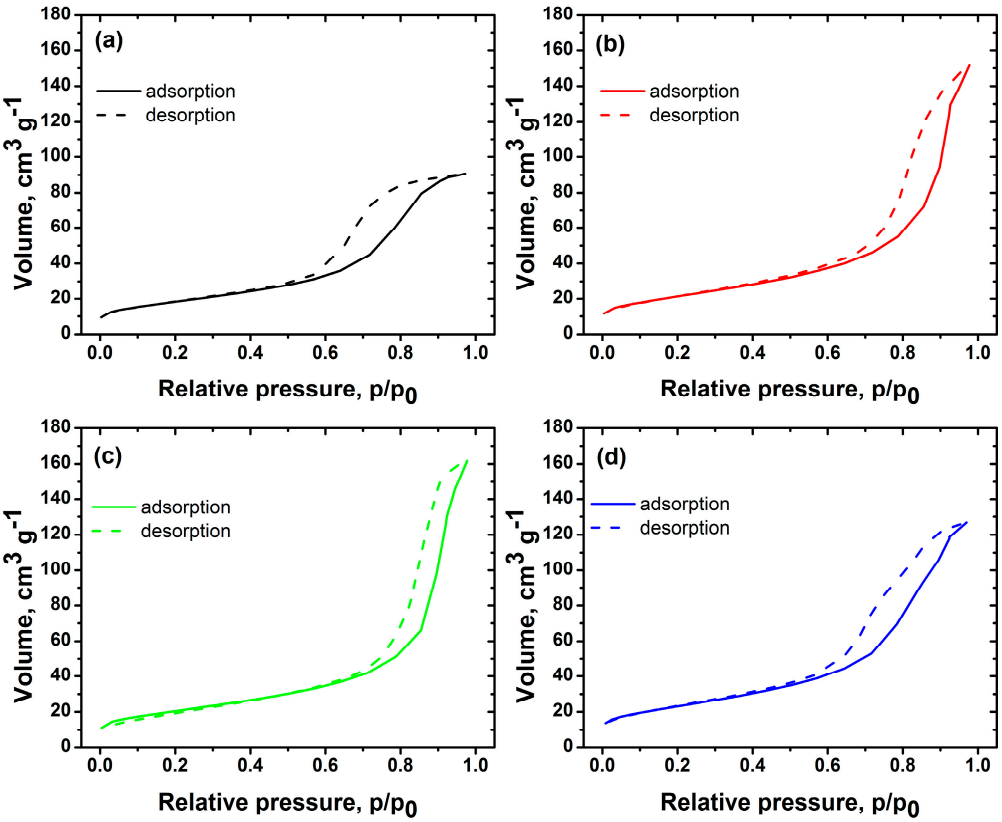

Figure 6. Brunauer–Emmett–Teller (BET) isotherms for zero-iron TiO_2 (**a**), 0.3 Fe-TiO_2 (**b**), 0.6 Fe-TiO_2 (**c**), and 1.0 Fe-TiO_2 (**d**).

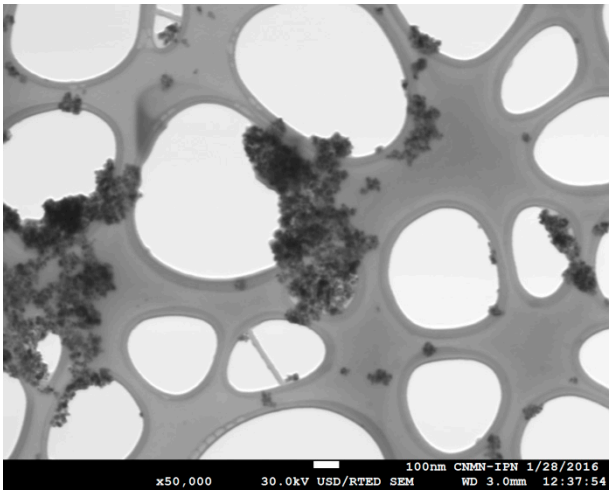

Figure 7. SEM image of zero-iron TiO_2 after mechanical grinding and sonication.

Transmission electron microscopy (TEM) images confirmed nanoparticle clusters and particle sizes of zero-iron TiO_2 (Figure 8b) and 0.3 Fe-TiO_2 (Figure 8a) between 5 and 10 nm (between 1.2 and 9.4 nm according to Scherrer's formula). The lattice fringe spacing was 0.35 nm, as shown in Figure 8b, which was consistent with the d-spacing (101) of anatase [25]. The lattice fingers of the nanoparticles showed that Fe-TiO_2 materials were highly crystallized.

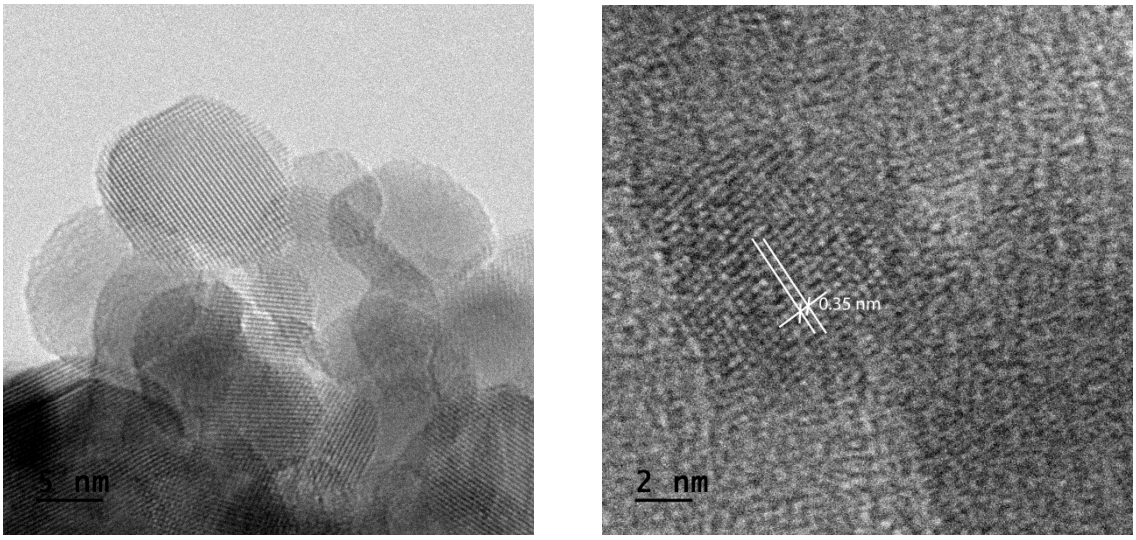

(**a**) (**b**)

Figure 8. Transmission electron microscopy (TEM) image of 0.3 Fe-TiO_2 (**a**) and zero-iron TiO_2 (**b**).

2.2. Characterization of Irradiation Source

Figure 9 shows the emission spectra of irradiation sources used in this study. Using the main peaks reported for a fluorescent lamp (Figure 9a), the calibration of the spectrometer generated an R^2 value equal to 0.999. The emission spectrum of the GE F15T8 BLB lamp (Figure 9b) was in the 356–410 nm range. However, the emission spectrum of the GE F15T8 D lamp (Figure 9c) was continuous broadband between 380 and 750 nm. The light intensity of the GE F15T8 lamp was reported to be between 3440 μW cm^{-2} [57] and 4000 μW cm^{-2} [58], from which 6% was UV radiation [59]. The intensity of the GE F15T8 lamp was 1500 μW cm^{-2}. This lamp has an internal coating that absorbs 78% of visible light (as specified by the manufacturer) in the spectrum below 400 nm, as shown in Figure 9b. Therefore, the GE F15T8 BLB and GE F15T8 D lamps were designated as high and low UV irradiation sources, respectively.

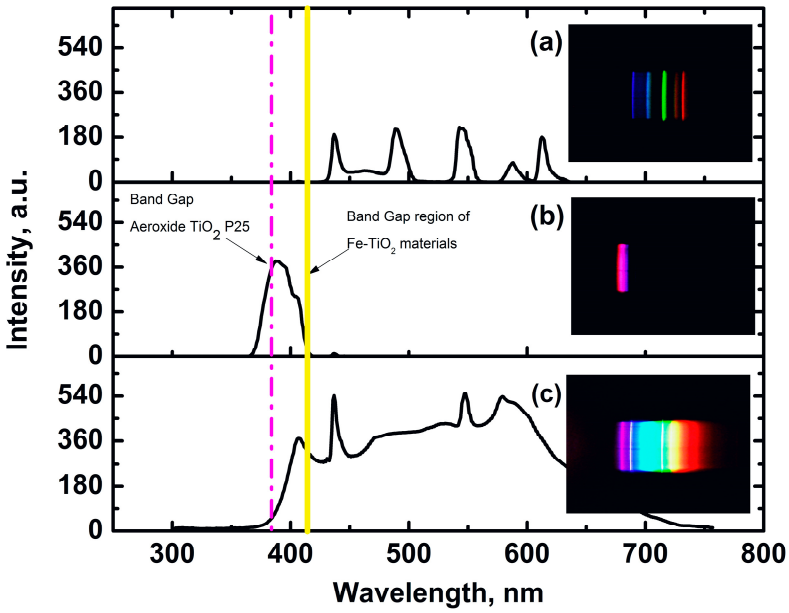

Figure 9. Emission spectrum and intensity graph of the irradiation source of Tecnolite fluorescent lamp (**a**), GE F15T8 BLB lamp (**b**), and GE F15T8 D lamp (**c**).

Because E_g of Aeroxide® TiO_2 P25 is 3.2 eV (387.5 nm), see Figure 9, both the GE F15T8 BLB and GE F15T8 D lamps emitted photons that could photoactivate Aeroxide® TiO_2 P25. However, the proportion of the emission spectrum that Aeroxide® TiO_2 P25 could use for photocatalytic activity was different. An approximation of the amount of radiative intensity used for photocatalytic activity was obtained with the area under the curve-spectrum below the E_g value. Consequently, Aeroxide® TiO_2 P25 could take advantage of 36.4% of the emission spectrum of the GE F15T8 BLB lamp and 0.8% of the emission spectrum of the GE F15T8 D lamp. Table 2 lists amount of radiative spectrum used by zero-iron TiO_2 and Fe-TiO_2 materials according to each E_g.

Based on morphological and crystalline structure analysis, the favorable characteristics to enhance photocatalytic activity of Fe-TiO_2 material are effective insertion of the Fe^{3+} ion into the TiO_2 lattice, red-shift (2.90–2.96 eV), nanoparticle size (6.9–7.1 nm), specific surface area (73.0–83.1 nm), pore size (1.2–9.4 nm), and radiation absorbance below the equivalent E_g wavelength (8.21–10.63% of daylight lamp spectrum). Its main disadvantageous characteristics are expected to be high particle agglomeration and lower anatase phase compared with zero-iron TiO_2. Further, photocatalytic activity is very sensitive to crystalline array and particle size and shape; differences in the density of hydroxyl groups on the particle surface and the number of water molecules hydrating the surface; the surface area and surface charge; differences in the number and nature of trap sites; the dopant concentration, localization, and chemical state of the dopant ions; radiation intensity; particle aggregation and superficial charge; and scavenger species in media [39,60]. Consequently, material characterization alone could not predict photocatalytic activity [28]. Therefore, in this research, we used the *N*,*N*-dimethyl-p-nitrosoaniline (pNDA) probe and E3 to evaluate the photocatalytic activity by following •OH production, which is one of the most significant reactive oxygen species (ROS), and E3, which is an EC.

2.3. Hydroxyl Radical Generation under High and Low UV Irradiation

The generation of •OH was measured using pNDA, which is a well-characterized •OH scavenger as mentioned in Section 3.5. In brief, pNDA undergoes bleaching when reacting with •OH according to Muff et al. mechanism of the oxidation of pNDA by •OH [61].

In this work, pNDA bleaching followed a pseudo-first-order equation, so the apparent rate constant was calculated by $\ln(C/C_0) = k_1 t$, where C_0 is the initial concentration, C is the reaction concentration at a given time, and k_1 is the pseudo-first-order reaction rate constant. The slope of the plot after applying a linear fit represents the rate constant, k_1.

Because the relationship between pNDA bleaching and •OH production follows a 1:1 stoichiometry [61], the steady-state of •OH generation ($[^{\bullet}OH]_{ss}$) can be considered equal to the initial velocity (r_0) according to Equation (1) and reported in Table 3:

$$\left.\frac{[\text{pNDA}]}{dt}\right|_{t=0} = r_0 = [^{\bullet}OH]_{ss} \quad (1)$$

Fe-TiO_2 materials showed a similar anatase:rutile phase ratio, particle size, and specific surface area, and therefore the variation in r_0 values was due to the difference of Fe content inside TiO_2. The generation of •OH radicals (r_0) was feasible using zero-iron TiO_2, Fe-TiO_2 materials, and Aeroxide® TiO_2 P25 under both high (Figure 10a) and low UV irradiation (Figure 10b).

Table 3. •OH generation rate of zero-iron TiO_2 and Fe-TiO_2.

Catalyst	at.%	Load	High UV Irradiation			Low UV Irradiation		
			k_1	R^2	r_0	k_1	R^2	r_0
		mg L^{-1}	min^{-1}		$\mu M_{\bullet OH}$ min^{-1}	min^{-1}		$\mu M_{\bullet OH}$ min^{-1}
TiO_2 Aeroxide® P25	-	20	0.06	0.988	0.49	0.012	0.989	0.105
Zero-iron TiO_2	0	320	0.056	0.993	0.49	0.005	0.973	0.045
0.3 Fe-TiO_2	0.3	320	0.067	0.998	0.58	0.004	0.990	0.042
0.6 Fe-TiO_2	0.6	320	0.031	0.998	0.28	0.002	0.999	0.025
1.0 Fe-TiO_2	1	320	0.004	0.987	0.04	0.00002	0.891	0.0002

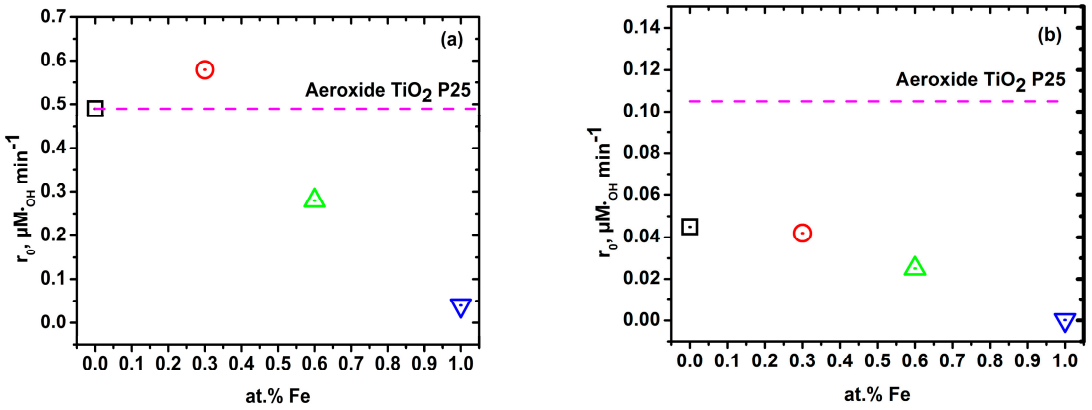

Figure 10. •OH generation (initial velocity) of zero-iron TiO_2 and Fe-TiO_2 under high UV irradiation (**a**) and low UV Irradiation (**b**); where ⊡ zero-iron TiO_2, ⊙ 0.3 Fe-TiO_2, △ 0.6 Fe-TiO_2, and 1.0 Fe-TiO_2 ▽ at pH 6 ± 0.1, and 20 °C.

When high UV irradiation was used, the maximum r_0 was 0.58 $\mu M_{\bullet OH}$ min^{-1} for 0.3 Fe-TiO_2. The enhancement in photocatalytic activity of 0.3 at.% Fe-TiO_2, compared with zero-iron TiO_2 was by the extended lifetime values of the photogenerated charge carriers (e^- and h^+) produced by Fe^{3+} ions, which played a role as charge carriers trapped at or near the particle surface. The trapping mechanisms are shown in Equations (2)–(5) [62].

$$Fe^{3+} + e_{cd}{}^- \rightarrow Fe^{2+} \quad \text{electron trap} \tag{2}$$

$$Fe^{2+} + Ti^{4+} \rightarrow Fe^{3+} + Ti^{3+} \quad \text{migration} \tag{3}$$

$$Fe^{3+} + h_{vb}{}^+ \rightarrow Fe^{4+} \quad \text{hole trap} \tag{4}$$

$$Fe^{4+} + OH^- \rightarrow Fe^{3+} + {}^\bullet OH \quad \text{migration} \tag{5}$$

The mechanism suggested for •OH generation is shown in Figure 11. When TiO_2 contains a Fe^{3+} ion, the Fe3d orbitals split into two bands, one is a hybrid band (A2g) and one is midgap band (T2g), which induce a new localized BG state [23]. Therefore, when TiO_2 absorbs photons with energy less than 3.2 eV, photoexcitation of the semiconductor promotes an electron from the VB to the midgap band (T2g), also called a shallow trap, creating an electron-hole pair. The hole in the valence band (VB) can react with hydroxide ions to form •OH, absorbed organic molecules, or trap Fe^{3+} following Equations (4) and (5). Additionally, photogenerated electrons in the midgap band (T2g) can be transferred to Fe^{3+} following a dark redox reaction at the interface, as suggested by Neubert et al. [63] and consequently bring about •OH.

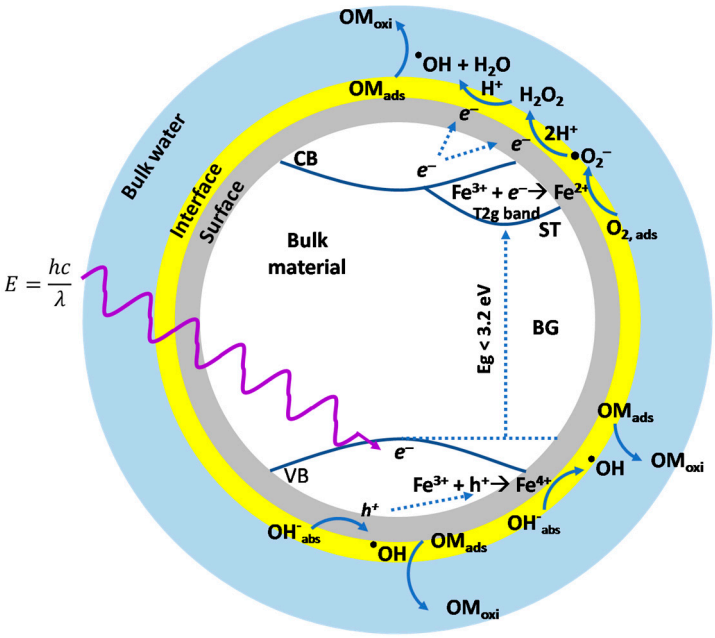

Figure 11. Photocatalytic mechanism of Fe-TiO_2 and $^{\bullet}OH$ generation. E_g is band gap energy, E is photon energy, OM_{ads} is adsorbed organic molecule, OM_{oxi} is oxidized organic molecule.

Increasing the Fe^{3+} doping content of Fe-TiO_2 to 0.6 and 1.0 at.%, Fe-TiO_2 was unfavorable to the photocatalytic activity because the additional Fe^{3+} doping in the TiO_2 sample inhibited the extended lifetime of charge carriers, acted as recombination sites and consequently decreased the photocatalytic efficiency [29], as proposed in Equations (6)–(9) [39].

$$Fe^{2+} + h_{vb}{}^{+} \rightarrow Fe^{3+} \quad \text{recombination} \tag{6}$$

$$Fe^{4+} + e_{cd}{}^{-} \rightarrow Fe^{3+} \quad \text{recombination} \tag{7}$$

$$Fe^{4+} + Fe^{2+} \rightarrow 2Fe^{3+} \quad \text{recombination} \tag{8}$$

$$Fe^{4+} + Ti^{3+} \rightarrow Fe^{3+} + Ti^{4+} \quad \text{recombination} \tag{9}$$

When low UV irradiation conditions were used, the r_0 values for zero-iron TiO_2 and Fe-TiO_2 materials were lower than the value estimated for Aeroxide® TiO_2 P25. Compared with the effects of high UV irradiation, the reduction in r_0 value observed was related both to pNDA adsorption of UV-visible radiation (lowered the number of photons available to activate the photocatalyst), and the augmented Fe content, which increased the recombination rate.

2.4. Photocatalytic Degradation of Estriol under High and Low UV Irradiation

E3 photocatalytic degradation curves are shown in Figure 12a,b using both high and low UV irradiation, respectively. In both cases, E3 photocatalytic degradation followed a pseudo-first-order model and the rate constant, k_1 (Table 4), was obtained by fitting experimental data to ln ([E3]/[$E3_0$]) = k_1t. Fe content influenced k_1 for both high and low UV irradiation.

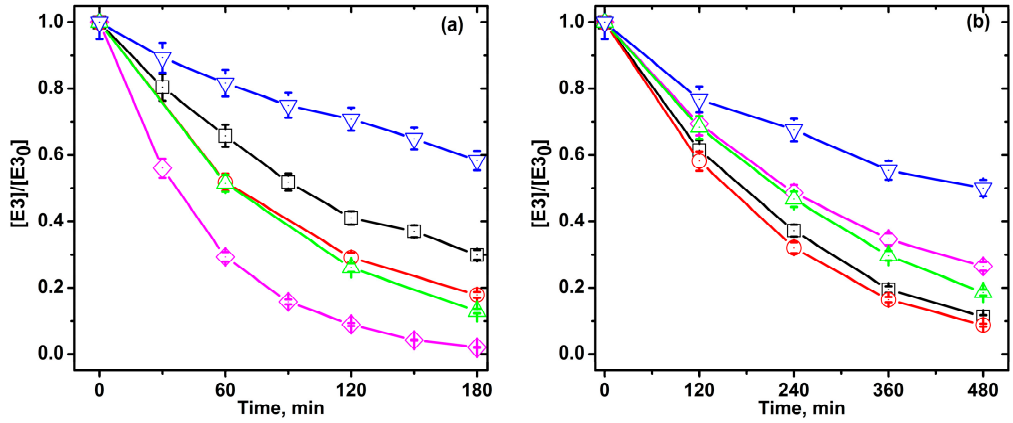

Figure 12. Photocatalytic degradation of E3 under high UV irradiation (**a**), and low UV irradiation (**b**); where ⊡ zero-iron TiO_2, ⊙ 0.3 Fe-TiO_2, △ 0.6 Fe-TiO_2, ▽ 1.0 Fe-TiO_2, and ◇ Aeroxide® TiO_2 P25; at pH 6 ± 0.1, and 20 °C.

Table 4. Kinetic values of E3 degradation using zero-iron TiO_2 and Fe-TiO_2.

Catalyst	Load	High UV Irradiation			Low UV Irradiation		
		k_1	R^2	$r_{0,E3}$	k_1	R^2	$r_{0,E3}$
	mg L^{-1}	min^{-1}		μM_{E3} min^{-1}	min^{-1}		μM_{E3} min^{-1}
TiO_2 Aeroxide® P25	20	0.021	0.996	0.21	0.0029	0.992	0.030
Zero-iron TiO_2	320	0.007	0.997	0.069	0.0045	0.991	0.040
0.3 Fe-TiO_2	320	0.009	0.994	0.090	0.0050	0.992	0.042
0.6 Fe-TiO_2	320	0.011	0.997	0.099	0.0034	0.999	0.030
1.0 Fe-TiO_2	320	0.003	0.979	0.027	0.0016	0.987	0.012

Figure 13 shows the pseudo-first-order rate constant (k_1) of E3 photocatalytic degradation. In general, the photocatalytic activity first increased and then decreased as the Fe concentration increased, which is similar to the behavior found with the •OH probe in Section 2.3 and has been previously reported using other organic molecules [23,29,64].

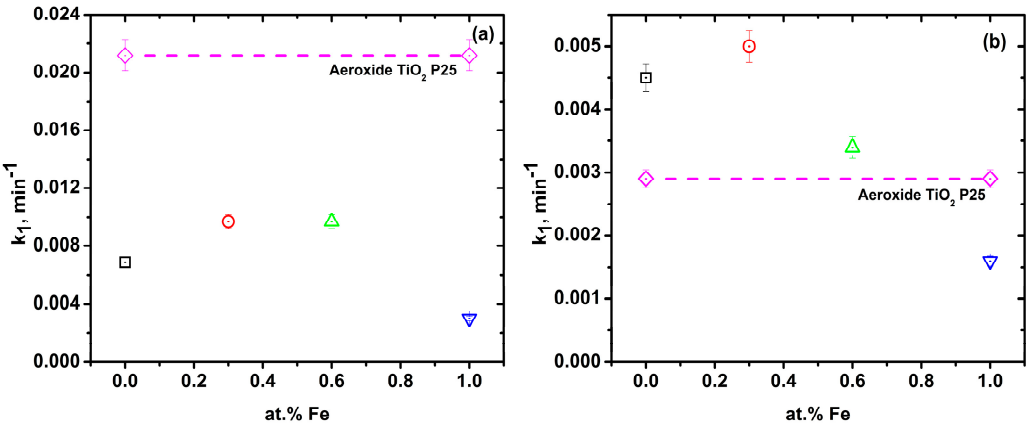

Figure 13. Photocatalytic reaction rate (k_1) for degradation of E3 under high UV irradiation (**a**), and low UV irradiation (**b**); where ⊡ zero-iron TiO_2, ⊙ 0.3 Fe-TiO_2, △ 0.6 Fe-TiO_2, and ▽ 1.0 Fe-TiO_2; at pH 6 ± 0.1, and 20 °C.

Under high UV irradiation (Figure 13a), 0.6 Fe-TiO_2 k_1 was higher than for zero-iron TiO_2, 0.3 Fe-TiO_2, and 1.0 Fe-TiO_2. The increase in photocatalytic performance of 0.6 Fe-TiO_2 was related with the increase in the lifetime of electron-hole pairs because Fe created additional energy levels near the conduction band of TiO_2, as the mechanism suggests in Figure 11.

Under low UV irradiation (Figure 13b), zero-iron TiO_2, 0.3 Fe-TiO_2, and 0.6 Fe-TiO_2 showed more photocatalytic activity than Aeroxide® TiO_2 P25 because those materials had enhanced superficial properties, such as particle size, and superficial area, as mentioned in Section 2.1. Furthermore, 0.3 Fe-TiO_2 enhanced photocatalytic activities with k_1 values as high as 0.005 min^{-1}. The high photocatalytic activity of 0.3 Fe-TiO_2 was due to the synergistic effect of unintentionally added co-dopants, superficial properties, and Fe content that increased the lifetime of photogenerated charge carriers and the efficiency of electron transfer.

The photocatalytic degradation rate of E3 using Aeroxide® TiO_2 P25 was reported to be 0.25 min^{-1} [65], 0.134 min^{-1} [66], and 0.12 min^{-1} [67]. However, the experimental setups and catalyst loads were different. Besides these few studies, E3 degradation using Fe-TiO_2 nanoparticles is scarcely reported. Only comparing magnitudes of k_1, the first-order rates to degrade pharmaceuticals using Fe-TiO_2 nanoparticles were 0.001 min^{-1} for ibuprofen, 0.0015 min^{-1} for carbamazepine, and 0.0014 min^{-1} for sulfamethoxazole [68], which are in the order of magnitude obtained in this work (see Table 4).

Regarding unintentionally added co-dopants, Fe-TiO_2 co-doping demonstrated a synergistic effect to increase photocatalytic activity under visible light for sulfur [69], nitrogen [44], and $Fe_xT_{i1-x}O_{2-y}N_y$ co-doping [70]. Surface properties of the material, such as a particle size (6.9 nm) and surface area (77.6 m^2 g^{-1}), also facilitated the mass transfer between interface, E3, and sub-products.

The relationship between the •OH radical system and E3 kinetic degradation was determined via linear fit between •OH initial rate generation ($r_{0,OH}$) and initial E3 degradation ($r_{0,E3}$). In general, the procedure to correlate $r_{0,OH}$ and $r_{0,E3}$ was first to sort pair values ($r_{0,OH}$, $r_{0,E3}$), and then fit the data to linear regression, as shown Figure 14a,b.

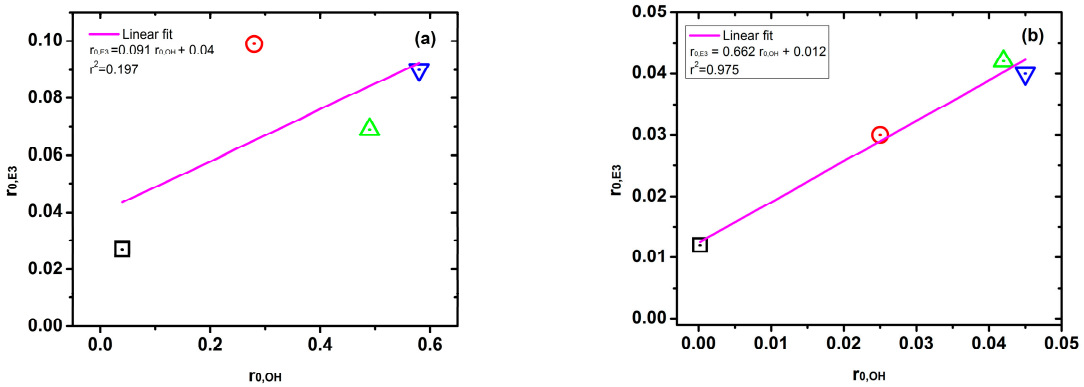

Figure 14. Correlation between •OH initial rate generation ($r_{0,OH}$) and initial E3 degradation ($r_{0,E3}$) under high UV irradiation (**a**), and low UV irradiation (**b**); where ⊡ zero-iron TiO_2, ⊙ 0.3 Fe-TiO_2, △ 0.6 Fe-TiO_2, and ▽ 1.0 Fe-TiO_2; at pH 6 ± 0.1, and 20 °C.

Under high UV irradiation, the linear fit correlation was $r_{0,E3} = 0.091\ r_{0,OH} + 0.040$ with $R^2 = 0.197$. Under low UV irradiation, the linear fit correlation was $r_{0,E3} = 0.066\ r_{0,OH} + 0.012$ with $R^2 = 0.975$. The correlation between the pair ($r_{0,OH}$, $r_{0,E3}$) under high UV irradiation was too low to be considered a linear relationship. We suggest the low correlation was because not only •OH caused E3 degradation, but holes (h^+) or other reactive oxygen species also caused E3 degradation.

However, a linear relationship under low UV irradiation was attributable to •OH being the main reactive oxygen species responsible for photocatalytic activity. Therefore, the contribution of h^+ to photocatalytic activity was lower because oxidation power was lower due to reduced E_g. This suggestion supports the mechanisms proposed in Figure 11, in which adding Fe into the lattice of TiO_2 reduced the E_g with a consistent reduction of redox potential, as mentioned by others [28].

The main mechanism of E3 degradation under low UV irradiation was via electron (e^-) transfer to give rise •OH. Additionally, the enhanced photocatalytic activity of 0.3 Fe-TiO_2 under low UV

irradiation provides evidence that the trapping-recombination mechanism of Fe-TiO_2 can be controlled by irradiation intensity. Therefore, we suggest that there is a trade-off between irradiation intensity, the trapping-recombination rate, and $^{\bullet}OH$ production that is worthy of further research.

The efficiency resource of the Fe-TiO_2/Low UV system was obtained through dimensional analysis of the slope of the linear fit of data shown in Figure 14b. The units of slope are E3 moles degraded per $^{\bullet}OH$ mol generated at initial time, so 0.662 E3 molecules underwent degradation when one $^{\bullet}OH$ was generated for the photocatalytic system independent of Fe doping content in TiO_2. A sustainable process was also achieved, for which 0.3 Fe-TiO_2 since absorbed 8.21% of emission spectra of the lamp below the equivalent E_g wavelength over 0.8% or 7.64% of Aeroxide® TiO_2 P25 and zero-iron TiO_2, respectively.

2.5. Relationship between Fe Content and Kinetic Constant

Photonic efficiency has been suggested to increase linearly with the doping ratio due to the formation of the charge carrier trapping centers, while it concurrently decreases quadratically with the doping ratio because to the creation of recombination centers [71]. Alternatively, we suggest an empirical relationship between the E3 degradation pseudo-first-order rate constant (k_1) and Fe content (at.%) in TiO_2, as described in Equation (10):

$$k_1(\delta) = c\left[e^{-k_e(\delta+\alpha)} - e^{-k_a(\delta+\alpha)}\right] \tag{10}$$

where k_1 is the pseudo-first-order constant, k_e is the electron trap constant, k_a is the electron recombination constant, δ at.% is the Fe doping amount in TiO_2, and c and α are system constants. To solve the model described in Equation (10), a numerical approximation by root-mean-square error minimization method was used according to Equation (11):

$$\varepsilon = \sqrt{\frac{1}{n}\sum_i \left|\overline{[k_{1.i}]} - [k_{1.i}]\right|} \tag{11}$$

where $\overline{[k_{1.i}]}$ is the theoretical k_1 value, $[k_{1.i}]$ is the experimental k_1 value, n is the number of data, and ε is the root-mean-square error. The solution of Equation (10) was performed by simultaneously solving k_e, k_a, c, and α using Excel Solver® (Frontline Systems, NV, US). As an example, photocatalytic degradation of E3 under low UV irradiation was fitted to Equation (10), as shown in Figure 15.

The empirical model solved in Equation (12) shows that electron trap constant (k_e) overcome electron recombination (k_a) before optimal catalyst load. This model could lead to experimental work using iron-doped TiO_2 in which the optimal content of Fe gives rise to the maximum E3 degradation.

$$k_1(\delta) = -1.99\left[e^{-2.81(\delta+0.197)} - e^{-2.78(\delta+0.197)}\right] \tag{12}$$

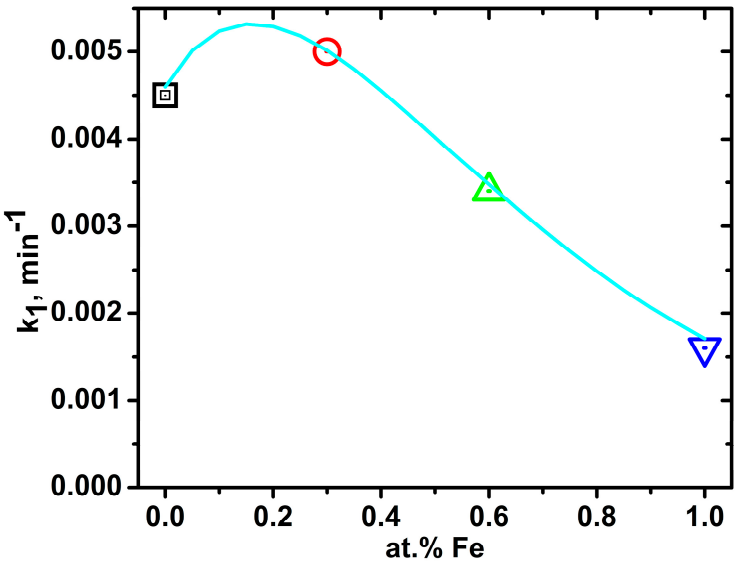

Figure 15. Experimental relationship between pseudo first order constant and at.% content; where ⊡ zero-iron TiO_2, ⊙ 0.3 Fe-TiO_2, △ 0.6 Fe-TiO_2, and ▽ 1.0 Fe-TiO_2; at pH 6 ± 0.1; and 20 °C.

3. Materials and Methods

3.1. Reagents

Sigma-Aldrich (St. Louis, MO, USA) supplied estriol (E3, $C_{18}H_{24}O_3$, ≥97%), titanium isopropoxide (TTIP, $Ti[OCH(CH_3)_2]_4$, 97%), *N*,*N*-Dimethyl-4-nitrosoaniline (pNDA, also called RNO, $C_8H_{10}N_{20}$, 97%), sodium dodecyl sulfate (SDS), and iron (III) nitrate ($Fe(NO_3)_3{\cdot}9H_2O$, >99.99%). Aeroxide® TiO_2 P25 (formerly Degussa P25 with 50 ± 15 m^2 g^{-1} of the specific surface area, 21 nm of average particle size, 80:20 of anatase:rutile ratio according to the manufacturer) granted by Evonik Industries (Essen, Germany) was the photocatalytic standard. Fremont (CA, USA) supplied HNO_3, H_2SO_4, absolute ethanol, HPLC-grade methanol, and HPLC-grade water. All chemicals were used as received.

3.2. Photoreactor Setup

Figure 16 depicts the photoreactor, which was a cylindrical water-jacketed glass vessel (318 mL) with 102 mm and 63 mm of interior height and diameter, respectively. The horizontal and vertical position of the photoreactor was constant for all experiments. Lamps were set horizontally and centered above the photoreactor. Two 15 W GE F15T8 BLB lamps (also called black-light lamps, Boston, MA, USA) supplied high UV irradiation, and two 15 W GE F15T8 D lamps (also called daylight lamps) provided low UV irradiation. The overall system was in a closed box to avoid the effects of sunlight or any artificial radiation sources. Lamp emission spectra were measured using a lab-made spectrophotometer using a CMOS webcam with a diffraction grating of 1000 lines mm^{-1} [72,73]. Emission spectra calibration of the spectrophotometer was developed using a 9 W fluorescent lamp (Tecnolite, Jalisco, Mexico). The temperature of all experiments was set at 20 °C using a thermostatic bath with recirculation (Polystat, Cole-Palmer, Vernon Hills, IL, USA). An optical filter was not used in the experiments, so visible light condition was not simulated.

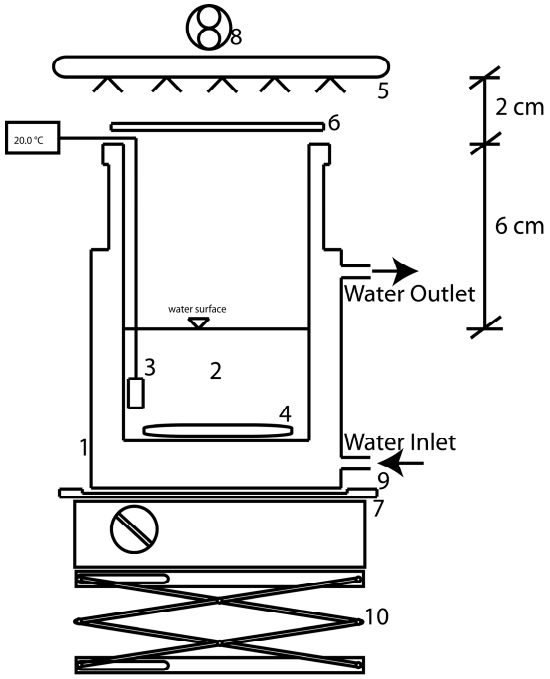

Figure 16. Scheme of photoreactor used for experiments: glass reactor (**1**), testing solution (**2**), temperature probe (**3**), spin bar (**4**), lamps (**5**), an optical filter (if needed) (**6**), stirring plate (**7**), cooling fan (**8**), horizontal position template (**9**), and lab jack lifting platform (**10**).

3.3. Synthesis of Materials

The synthesis method of iron-doped TiO_2 (Fe-TiO_2) materials followed the hydrothermal sol-gel synthetic approach proposed by Patra et al. with some differences in precursor and thermal treatment [49]. Our synthesis method used iron (III) nitrate instead of $FeCl_3$ and absolute ethanol instead of isopropyl alcohol. The thermal treatment was a programmed cycle of 31 h (increasing ramp-drying-increasing ramp-calcination-decreasing ramp) instead of direct calcination for 6 h. First, solution A was prepared by dissolving 1.44 g of SDS in 10 mL of deionized water. Then, four different solutions B were prepared to dissolve iron (III) nitrate in 2 mL of absolute ethanol ($\geq$99.8 %) and 3 mL of TTIP was added slowly. The amounts of iron (III) nitrate were 0, 0.4, 4.3, and 42.6 mg of $Fe(NO_3)_3 \cdot 9H_2O$ identified as zero-iron TiO_2, 0.3 Fe-TiO_2, 0.6 Fe-TiO_2, and 1.0 Fe-TiO_2, respectively. Once ready, solution A was continuously stirred and solution B was slowly dropped into solution A. The pH of the resulting mixture was adjusted to 1 using concentrated HNO_3 and stirred for 3 h. The mixture was kept at 3 °C for 36 h. The precipitated solid was collected by filtration using Whatman Quantitative Filter Paper Grade 42. The materials were simultaneously dried and calcinated with a programmed thermal treatment (Isotemp® Programmable Muffle Furnace, Fisher Scientific, Dubuque, IA, USA) following first the temperature increase from ambient temperature to 353 K, with a temperature ramp of 1 K min^{-1} that was held for 720 min. The temperature was then increased from 353 K to 773 K with a temperature ramp of 1 K min^{-1} that was held for 360 min. Finally, the temperature was decreased from 773 K to 353 K with a temperature ramp of -1 K min^{-1}, and then the furnace was turned off. The materials were washed with 50:50 methanol-water and dried to 377 K overnight.

3.4. Materials Characterization

X-ray photoelectron spectroscopy (XPS) was performed using a Thermo Fisher Scientific K-Alpha X-ray photoelectron spectrometer (Waltham, MA, USA) with a monochromatized Al K_α X-ray source (1487 V). The deconvolution of high-resolution XPS spectra was developed using the software XPSpeak 4.1. (Raymund W.M. Kwok, Shatin, Hong Kong).

UV-visible reflectance spectroscopy was obtained with Video–Barrelino integrating sphere coupled to Cary 50 spectrophotometer (Varian Inc, Palo Alto, CA, USA). Diffuse reflectance spectra were transformed using the Kubelka–Munk method to obtain E_g of zero-iron TiO_2 and Fe-TiO_2 materials. Kubelka–Munk method plots $(F(R)hv)^{1/2}$ versus hv, draws a tangent at the inflection point on the curve and estimates E_g with the hv value at the intersection with abscissa. In this case, F(R) is a reflectance function equal to $(1 - R)^2/2R$, R is the reflectance percentage, h is the Planck's constant, and v is frequency.

XRD patterns were recorded in a Siemens D-5000 diffractometer (Munich, Germany) using Cu K_α radiation (λ = 1.54060 Å) from 10° to 85°. The procedure for phase identification used the QualX2.0 software with database developed by Altomare et al. [74]. The cards used for identification were 00-901-5929, 00-900-1681, and 00-900-4140 for anatase, rutile, and brookite, respectively. The quantification phases followed the method proposed by Spurr and Myers according to Equation (13):

$$f = \frac{1}{1 + 1.26\frac{I_R}{I_A}} \quad (13)$$

where f is the anatase percentage, I_A is intensity at a diffraction angle 2θ of 25.36°, and I_R is intensity at a diffraction angle 2θ of 27.46° [75].

The particle size was estimated by Scherrer's formula described in Equation (14), where β is the full width at half of the maximum of the diffraction peaks (radians), k is the shape constant, λ is the wavelength of the incident Cu K_α radiation (λ = 1.54060 Å), θ is the Bragg's angle (radians), and D is the particle size (Å).

$$D = \frac{k\,\lambda}{\beta\,\cos\theta} \quad (14)$$

Brunauer–Emmett–Teller (BET) isotherms were obtained in Nova Station A equipment (Quantachrome Instruments, Boynton Beach, FL, USA). The surface morphology was observed by SEM in a JEOL ultrahigh resolution field emission electron microscope JSM-7800 F (JEOL, Tokyo, Japan) with 20 kV accelerating voltage, and 3 mm WD. Transmission electron microscopy (TEM) images were obtained in a JEM-2100 LaB6 electron microscope (JEOL, Tokyo, Japan).

3.5. Hydroxyl Radical Generation

In this study, pNDA bleaching was selected as an •OH probe because pNDA was useful for measuring the photocatalytic performance of TiO_2 [51,76,77] because of the following advantages: (1) it is selective of the reaction of pNDA with •OH [78]; (2) its high reaction rate with •OH on the order of 10^{10} M^{-1} s^{-1} [51,79]; (3) its easy application through observable bleaching at 440 nm following Beer's Law, in which pNDA bleaching a yellowish solution to transparent; and (4) its 1:1 stoichiometry, meaning that one •OH can bleach one pNDA molecule [51,80–82].

The pNDA absorption (Figure 17) measurements were obtained using a UV-visible spectrophotometer (Hatch DR/4000U, Loveland, CO, USA) at 440 nm following Beer-Lambert law. The pNDA test solution was 10 μM initial concentration and pH 6.0 ± 0.1 adjusted using NaOH or HCl when needed. No buffer solutions were used because they can compete for •OH. Final pH was verified at the end of tests to discharge pH-pNDA bleaching.

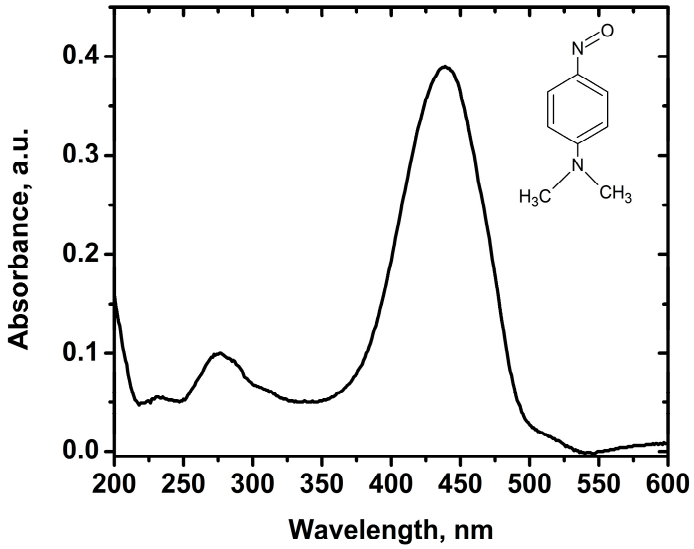

Figure 17. Structural formula and absorbance spectrum of *N*,*N*-dimethyl-p-nitrosoaniline (pNDA).

The photocatalytic standard was Aeroxide® TiO_2 P25, and the load was 20 mg L^{-1}. The choice of catalyst load was based on our previous work on •OH generation of Aeroxide® TiO_2 P25 [16]. For zero-iron TiO_2 and Fe-TiO_2 materials, the catalyst load used was 320 mg L^{-1}, which produced a •OH generation rate under high UV irradiation to set a baseline. Catalyst load differences were attributable to the aggregation of lab-made TiO_2, superficial properties, and optical properties of suspensions, as shown in Figure 18.

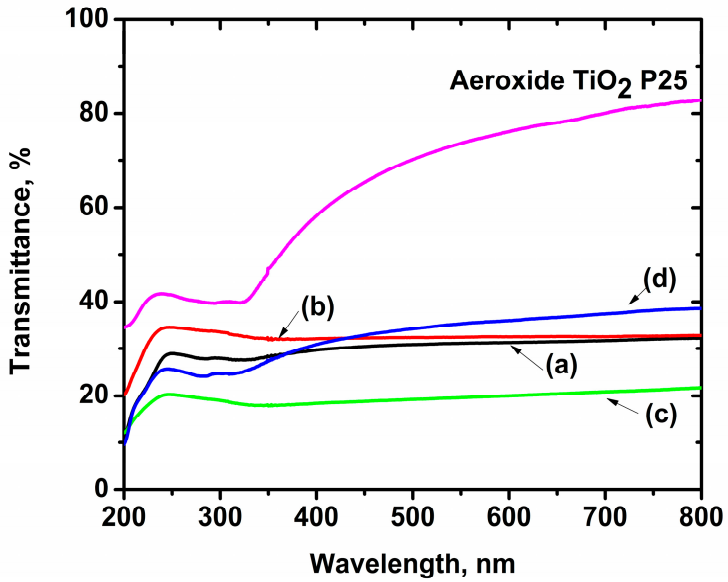

Figure 18. Suspension transmittance of Fe-TiO_2 material and Aeroxide TiO_2 P25; where zero-iron TiO_2 (**a**), 0.3 Fe-TiO_2 (**b**), 0.6 Fe-TiO_2 (**c**), and 1.0 Fe-TiO_2 (**d**).

The photocatalytic experiments were conducted as follows. First, a pNDA test solution was set at 20 °C, the catalyst was added, and the suspension was mixed for 20 min without radiation. To evaluate the adsorption of pNDA on TiO_2, an aliquot was withdrawn and centrifuged. Then, the system was fully illuminated, and aliquots were withdrawn after specific periods. Each sample was centrifuged at 6000 rpm for 15 min (Biofuge Primo, Sorvall, Hanau, Germany) and measured in the UV-visible spectrophotometer. Once the catalyst load was used and after the dark phase, no adsorption of pNDA was detected near the detection limit of UV-visible spectrophotometer.

3.6. Photolysis and Photocatalytic Degradation of E3

The initial E3 concentration was 10 μM because (1) this research was part of a project focused on the removal of E3 in water using sequentially coupled membrane filtration; (2) the solubility limit of E3 in water was previously reported to be 11.1 μM [83], and 45.1 μM [8,84], and (3) the sensitivity of the analytical techniques used in this work. The E3 solution was prepared to dissolve 2.88 mg of E3 in 1 L of deionized water by stirring at room conditions in the dark for six hours. Working solutions were stored in an amber flask.

Each photocatalytic experiment used 100 mL of E3 working solution. Initial pH was adjusted to obtain a similar surface charge of TiO_2 [85]. Depending on the initial water conditions, the initial pH value was adjusted to 6.0 ± 0.1 using NaOH or HCl when needed. A dark period (no radiation) was allowed for 20 min. Then, similar experimental conditions were carried out as described in Section 3.5. Additionally, the aliquots withdrawn from suspension were filtered using a 0.1 μm syringe filter (MillexVV, Millipore, Billerica, MA, USA). A blank experiment without irradiation and TiO_2 photocatalyst was conducted for comparison. The blank experiment showed that E3 cannot be degraded in absences of either TiO_2 or UV light. Once the catalyst was loaded and after the dark phase, no adsorption of E3 was detected near the detection limit of HPLC.

3.7. Analytical Methods

The E3 concentration was monitored using an HPLC system (Waters 1515; Milford, MA, USA) equipped with a UV detector (Waters 2787) that has an injection volume of 20 μL. The analytical method was performed in isocratic analytical mode using an Inertsil® ODS-3 column (GL Science, Tokyo, Japan; 150 mm × 4.6 mm, 5 μm) thermostated at 25 °C. The wavelength was at 280 nm according to E3 maximum absorbance. The mobile phase was methanol (49%) and deionized water (51%) at a flow rate of 1 mL min^{-1}. The retention time of E3 was 10 min, and the limit of E3 detection was 0.1 μM (0.029 mg L^{-1}). The detection limit was obtained by developing two calibration curves: the first between 10 and 0.1 and second between 1 and 0.01. Both calibration curves followed area = 2928[E3] with R^2 = 0.9899, but areas below 0.1 were not detected.

4. Conclusions

This study provided an understanding of the relationship between the Fe doping ratio and radiation intensity for •OH generation and estriol (E3) degradation. The main results were that:

- E3 degradation using 0.3 Fe-TiO_2 was feasible and can be improved by controlling irradiation intensity which was found closely related with light absorption and the catalytic reaction rate;
- the synthesis method and thermal treatment allowed nanoparticles with large superficial areas and the incorporation of iron ions into the TiO_2 lattice.; and
- changes in trapping recombination centers could be controlled with irradiation intensity to enhance the photocatalytic activity.

Therefore, our findings provide the opportunity to reconsider studies in which iron-doped TiO_2 impaired photocatalytic activity and to improve an application in which irradiation should be controlled. For example, Fe-TiO_2 can potentially be applied to medical uses in which low irradiation intensity should be used to avoid adverse effects in humans or wildlife, which has also been suggested by others [86]. In the field of water treatment, we propose that Fe-TiO_2 is an efficient material that could harvest low-energy photons to degrade and mineralize dyes [87], biocides [88], pharmaceuticals [89], industrial chemicals [90], and estrogens—as shown in this study—to create an energetically green water treatment process.

Author Contributions: Funding acquisition, E.R.B.; Investigation, I.M.R.-S.; Project administration, E.R.B.; Supervision, E.R.B.; Writing—original draft, I.M.R.-S.; Writing—review & editing, E.R.B.

Funding: This manuscript is based on work supported in part by ConTex postdoctoral program, which is an initiative of the University of Texas System and Mexico's National Council of Science and Technology (CONACYT). The research was partially funded by CONACYT under Project CB-2011/168285. The APC was funded by the Institutional Open Access Program (IAOP) between The University of Texas at Austin and Desert Research Institute (DRI) at Nevada.

Acknowledgments: The Aeroxide® P25 Evonik catalyst used for this work was provided by Intertrade S.A. de C.V., the supplier of Evonik Industries in Mexico. The authors thank L. Lartundo-Rojas, Raul Borja Urbi, Hugo Martinez Gutiérrez, and Joao Jairzinho Salinas Camargo for assistance in XPS spectroscopy, TEM images, SEM images, and absorption isotherms, respectively, all of whom are from Centro de Nanociencias y Micro y Nanotecnología (CNMN) of IPN, Mexico. The authors thank M.A. Quiroz Alfaro for his excellent technical help and for his permission to use materials and equipment at the UDLAP's electrochemical lab. The authors also thank Nicole Damon (DRI) for her editorial review.

Conflicts of Interest: The authors declare no conflict of interest.

References

1. Dulio, V.; van Bavel, B.; Brorström-Lundén, E.; Harmsen, J.; Hollender, J.; Schlabach, M.; Slobodnik, J.; Thomas, K.; Koschorreck, J. Emerging pollutants in the EU: 10 years of NORMAN in support of environmental policies and regulations. *Environ. Sci. Eur.* **2018**, *30*, 5. [CrossRef]
2. Mandaric, L.; Celic, M.; Marcé, R.; Petrovic, M. Introduction on Emerging Contaminants in Rivers and Their Environmental Risk. In *Emerging Contaminants in River Ecosystems: Occurrence and Effects under Multiple Stress Conditions*; Petrovic, M., Sabater, S., Elosegi, A., Barceló, D., Eds.; Springer International Publishing: Cham, Switzerland, 2016; pp. 3–25. ISBN 978-3-319-29376-9.
3. Houtman, C.J.; Legler, J.; Thomas, K. *Effect-Directed Analysis of Complex Environmental Contamination*; Brack, W., Ed.; Springer: Berlin/Heidelberg, Germany, 2011; pp. 237–265. ISBN 978-3-642-18384-3.
4. Dimogerontas, G.; Liapi, C. Endocrine Disruptors (Xenoestrogens): An Overview. In *Plastics in Dentistry and Estrogenicity: A Guide to Safe Practice*; Eliades, T., Eliades, G., Eds.; Springer: Berlin/Heidelberg, Germany, 2014; pp. 3–48. ISBN 978-3-642-29687-1.
5. Hileman, B. Environmental Estrogens linked to Reproductive Abnormalities, Cancer. *Chem. Eng. News Arch.* **1994**, *72*, 19–23. [CrossRef]
6. Prat, N.; Rieradevall, M.; Barata, C.; Munné, A. The combined use of metrics of biological quality and biomarkers to detect the effects of reclaimed water on macroinvertebrate assemblages in the lower part of a polluted Mediterranean river (Llobregat River, NE Spain). *Ecol. Indic.* **2013**, *24*, 167–176. [CrossRef]
7. Souza, M.S.; Hallgren, P.; Balseiro, E.; Hansson, L.A. Low concentrations, potential ecological consequences: Synthetic estrogens alter life-history and demographic structures of aquatic invertebrates. *Environ. Pollut.* **2013**, *178*, 237–243. [CrossRef]
8. Silva, C.P.; Otero, M.; Esteves, V. Processes for the elimination of estrogenic steroid hormones from water: A review. *Environ. Pollut.* **2012**, *165*, 38–58. [CrossRef]
9. Rodriguez-Narvaez, O.M.; Peralta-Hernandez, J.M.; Goonetilleke, A.; Bandala, E.R. Treatment technologies for emerging contaminants in water: A review. *Chem. Eng. J.* **2017**, *323*, 361–380. [CrossRef]
10. Gągol, M.; Przyjazny, A.; Boczkaj, G. Wastewater treatment by means of advanced oxidation processes based on cavitation—A review. *Chem. Eng. J.* **2018**, *338*, 599–627. [CrossRef]
11. Boczkaj, G.; Fernandes, A. Wastewater treatment by means of advanced oxidation processes at basic pH conditions: A review. *Chem. Eng. J.* **2017**, *320*, 608–633. [CrossRef]
12. Coleman; Eggins, B.; Byrne, J.A.; Palmer, F.L.; King, E. Photocatalytic degradation of 17-β-oestradiol on immobilised TiO_2. *Appl. Catal. B Environ.* **2000**, *24*, L1–L5. [CrossRef]
13. Ramirez-Sanchez, I.M.; Mendez-Rojas, M.A.; Bandala, E.R. CHAPTER 25 Photocatalytic Degradation of Natural and Synthetic Estrogens with Semiconducting Nanoparticles. In *Advanced Environmental Analysis: Applications of Nanomaterials*; The Royal Society of Chemistry: London, UK, 2017; Volume 2, pp. 153–177. ISBN 978-1-78262-906-1.
14. Ohko, Y.; Iuchi, K.; Niwa, C.; Tatsuma, T.; Nakashima, T.; Iguchi, T.; Kubota, Y.; Fujishima, A. 17β-Estradiol Degradation by TiO_2 Photocatalysis as a Means of Reducing Estrogenic Activity. *Environ. Sci. Technol.* **2002**, *36*, 4175–4181. [CrossRef]

15. Coleman, H.M.; Routledge, E.J.; Sumpter, J.P.; Eggins, B.R.; Byrne, J.A. Rapid loss of estrogenicity of steroid estrogens by UVA photolysis and photocatalysis over an immobilised titanium dioxide catalyst. *Water Res.* **2004**, *38*, 3233–3240. [CrossRef]
16. Ramírez-Sánchez, I.M.; Tuberty, S.; Hambourger, M.; Bandala, E.R. Resource efficiency analysis for photocatalytic degradation and mineralization of estriol using TiO_2 nanoparticles. *Chemosphere* **2017**, *184*, 1270–1285. [CrossRef]
17. Hashimoto, K.; Irie, H.; Fujishima, A. Photocatalysis: A Historical Overview and Future Prospects. *Jpn. J. Appl. Phys.* **2005**, *44*, 8269–8285. [CrossRef]
18. Fujishima, A.; Zhang, X.; Tryk, D.A. TiO_2 photocatalysis and related surface phenomena. *Surf. Sci. Rep.* **2008**, *63*, 515–582. [CrossRef]
19. Tong, A.Y.C.; Braund, R.; Warren, D.S.; Peake, B.M. TiO_2-assisted photodegradation of pharmaceuticals—A review. *Cent. Eur. J. Chem.* **2012**, *10*, 989–1027. [CrossRef]
20. Cassaignon, S.; Colbeau-Justin, C.; Durupthy, O. Titanium dioxide in photocatalysis. In *Nanomaterials: A Danger or a Promise?: A Chemical and Biological Perspective*; Springer: London, UK, 2013; pp. 153–188. ISBN 9781447142133.
21. Augugliaro, V.; Loddo, V.; Pagliaro, M.; Palmisano, G.; Palmisano, L. *Clean by Light Irradiation: Practical Applications of Supported TiO2*; RSC Publishing: Cambridge, UK, 2010; ISBN 1847558704.
22. Etacheri, V.; Di Valentin, C.; Schneider, J.; Bahnemann, D.; Pillai, S.C. Visible-light activation of TiO_2 photocatalysts: Advances in theory and experiments. *J. Photochem. Photobiol. C Photochem. Rev.* **2015**, *25*, 1–29. [CrossRef]
23. Wen, L.; Liu, B.; Zhao, X.; Nakata, K.; Murakami, T.; Fujishima, A. Synthesis, Characterization, and Photocatalysis of Fe-Doped TiO_2: A Combined Experimental and Theoretical Study. *Int. J. Photoenergy* **2012**, *2012*, 1–10. [CrossRef]
24. Yu, H.; Irie, H.; Hashimoto, K. Conduction band energy level control of titanium dioxide: Toward an efficient visible-light-sensitive photocatalyst. *J. Am. Chem. Soc.* **2010**, *132*, 6898–6899. [CrossRef]
25. Choi, W.; Termin, A.; Hoffmann, M.R. The role of metal ion dopants in quantum-sized TiO_2: Correlation between photoreactivity and charge carrier recombination dynamics. *J. Phys. Chem.* **1994**, *98*, 13669–13679. [CrossRef]
26. Kaur, T.; Sraw, A.; Wanchoo, R.K.; Toor, A.P. Visible–Light Induced Photocatalytic Degradation of Fungicide with Fe and Si Doped TiO_2 Nanoparticles. *Mater. Today Proc.* **2016**, *3*, 354–361. [CrossRef]
27. Zhao, B.; Mele, G.; Pio, I.; Li, J.; Palmisano, L.; Vasapollo, G. Degradation of 4-nitrophenol (4-NP) using Fe-TiO_2 as a heterogeneous photo-Fenton catalyst. *J. Hazard. Mater.* **2010**, *176*, 569–574. [CrossRef]
28. Yalçın, Y.; Kılıç, M.; Çınar, Z. Fe^{+3}-doped TiO_2: A combined experimental and computational approach to the evaluation of visible light activity. *Appl. Catal. B Environ.* **2010**, *99*, 469–477. [CrossRef]
29. Cai, L.; Liao, X.; Shi, B. Using Collagen Fiber as a Template to Synthesize TiO_2 and Fe_x/TiO_2 Nanofibers and Their Catalytic Behaviors on the Visible Light-Assisted Degradation of Orange II. *Ind. Eng. Chem. Res.* **2010**, *49*, 3194–3199. [CrossRef]
30. Li, J.; Xu, J.; Dai, W.L.; Li, H.; Fan, K. Direct hydro-alcohol thermal synthesis of special core-shell structured Fe-doped titania microspheres with extended visible light response and enhanced photoactivity. *Appl. Catal. B Environ.* **2009**, *85*, 162–170. [CrossRef]
31. Tong, T.; Zhang, J.; Tian, B.; Chen, F.; He, D. Preparation of Fe^{3+}-doped TiO_2 catalysts by controlled hydrolysis of titanium alkoxide and study on their photocatalytic activity for methyl orange degradation. *J. Hazard. Mater.* **2008**, *155*, 572–579. [CrossRef]
32. Ambrus, Z.; Balázs, N.; Alapi, T.; Wittmann, G.; Sipos, P.; Dombi, A.; Mogyorósi, K. Synthesis, structure and photocatalytic properties of Fe(III)-doped TiO_2 prepared from $TiCl_3$. *Appl. Catal. B Environ.* **2008**, *81*, 27–37. [CrossRef]
33. Cong, Y.; Zhang, J.; Chen, F.; Anpo, M.; He, D. Preparation, photocatalytic activity, and mechanism of nano-TiO_2 Co-doped with nitrogen and iron (III). *J. Phys. Chem. C* **2007**, *111*, 10618–10623. [CrossRef]
34. Adán, C.; Bahamonde, A.; Fernández-García, M.; Martínez-Arias, A. Structure and activity of nanosized iron-doped anatase TiO_2 catalysts for phenol photocatalytic degradation. *Appl. Catal. B Environ.* **2007**, *72*, 11–17. [CrossRef]

35. Yamashita, H.; Harada, M.; Misaka, J.; Takeuchi, M.; Neppolian, B.; Anpo, M. Photocatalytic degradation of organic compounds diluted in water using visible light-responsive metal ion-implanted TiO_2 catalysts: Fe ion-implanted TiO_2. *Catal. Today* **2003**, *84*, 191–196. [CrossRef]
36. Li, X.; Yue, P.-L.; Kutal, C. Synthesis and photocatalytic oxidation properties of iron doped titanium dioxide nanosemiconductor particles. *New J. Chem.* **2003**, *27*, 1264. [CrossRef]
37. Zhang, Z.; Wang, C.-C.; Zakaria, R.; Ying, J.Y. Role of Particle Size in Nanocrystalline TiO_2-Based Photocatalysts. *J. Phys. Chem. B* **1998**, *102*, 10871–10878. [CrossRef]
38. Litter, M.I.; Navío, J.A. Photocatalytic properties of iron-doped titania semiconductors. *J. Photochem. Photobiol. A Chem.* **1996**, *98*, 171–181. [CrossRef]
39. Fàbrega, C.; Andreu, T.; Cabot, A.; Morante, J.R. Location and catalytic role of iron species in TiO_2:Fe photocatalysts: An EPR study. *J. Photochem. Photobiol. A Chem.* **2010**, *211*, 170–175. [CrossRef]
40. Seabra, M.P.; Salvado, I.M.M.; Labrincha, J.A. Pure and (zinc or iron) doped titania powders prepared by sol-gel and used as photocatalyst. *Ceram. Int.* **2011**, *37*, 3317–3322. [CrossRef]
41. Abazović, N.D.; Mirenghi, L.; Janković, I.A.; Bibić, N.; Šojić, D.V.; Abramović, B.F.; Čomor, M.I. Synthesis and characterization of rutile TiO_2 nanopowders doped with iron ions. *Nanoscale Res. Lett.* **2009**, *4*, 518–525. [CrossRef]
42. Geissen, V.; Mol, H.; Klumpp, E.; Umlauf, G.; Nadal, M.; van der Ploeg, M.; van de Zee, S.E.A.T.M.; Ritsema, C.J. Emerging pollutants in the environment: A challenge for water resource management. *Int. Soil Water Conserv. Res.* **2015**, *3*, 57–65. [CrossRef]
43. Lin, T.C.; Seshadri, G.; Kelber, J.A. A consistent method for quantitative XPS peak analysis of thin oxide films on clean polycrystalline iron surfaces. *Appl. Surf. Sci.* **1997**, *119*, 83–92. [CrossRef]
44. Xing, M.; Wu, Y.; Zhang, J.; Chen, F. Effect of synergy on the visible light activity of B, N and Fe co-doped TiO_2 for the degradation of MO. *Nanoscale* **2010**, *2*, 1233. [CrossRef] [PubMed]
45. Lopez, R.; Gomez, R. Band-gap energy estimation from diffuse reflectance measurements on sol-gel and commercial TiO_2: A comparative study. *J. Sol-Gel Sci. Technol.* **2012**, *61*, 1–7. [CrossRef]
46. Shi, J.; Chen, G.; Zeng, G.; Chen, A.; He, K.; Huang, Z.; Hu, L.; Zeng, J.; Wu, J.; Liu, W. Hydrothermal synthesis of graphene wrapped Fe-doped TiO_2 nanospheres with high photocatalysis performance. *Ceram. Int.* **2018**, *44*, 7473–7480. [CrossRef]
47. Yu, J.; Xiang, Q.; Zhou, M. Preparation, characterization and visible-light-driven photocatalytic activity of Fe-doped titania nanorods and first-principles study for electronic structures. *Appl. Catal. B Environ.* **2009**, *90*, 595–602. [CrossRef]
48. Goswami, P.; Ganguli, J.N. Evaluating the potential of a new titania precursor for the synthesis of mesoporous Fe-doped titania with enhanced photocatalytic activity. *Mater. Res. Bull.* **2012**, *47*, 2077–2084. [CrossRef]
49. Patra, A.K.; Dutta, A.; Bhaumik, A. Highly ordered mesoporous TiO_2-Fe_2O_3 mixed oxide synthesized by sol-gel pathway: An efficient and reusable heterogeneous catalyst for dehalogenation reaction. *ACS Appl. Mater. Interfaces* **2012**, *4*, 5022–5028. [CrossRef] [PubMed]
50. Luttrell, T.; Halpegamage, S.; Tao, J.; Kramer, A.; Sutter, E.; Batzill, M. Why is anatase a better photocatalyst than rutile?—Model studies on epitaxial TiO_2 films. *Sci. Rep.* **2014**, *4*, 4043. [CrossRef] [PubMed]
51. Zang, L.; Qu, P.; Zhao, J.; Shen, T.; Hidaka, H. Photocatalytic bleaching of p-nitrosodimethylaniline in TiO_2 aqueous suspensions: A kinetic treatment involving some primary events photoinduced on the particle surface. *J. Mol. Catal. A Chem.* **1997**, *120*, 235–245. [CrossRef]
52. Othman, S.H.; Abdul Rashid, S.; Mohd Ghazi, T.I.; Abdullah, N. Fe-Doped TiO_2 Nanoparticles Produced via MOCVD: Synthesis, Characterization, and Photocatalytic Activity. *J. Nanomater.* **2011**, *2011*, 1–8. [CrossRef]
53. Teoh, W.Y.; Amal, R.; Mädler, L.; Pratsinis, S.E. Flame sprayed visible light-active Fe-TiO_2 for photomineralisation of oxalic acid. *Catal. Today* **2007**, *120*, 203–213. [CrossRef]
54. Pongwan, P.; Inceesungvorn, B.; Wetchakun, K.; Phanichphant, S.; Wetchakun, N. Highly efficient visible-light-induced photocatalytic activity of Fe-doped TiO_2 nanoparticles. *Eng. J.* **2012**, *16*, 143–151. [CrossRef]
55. Kruk, M.; Jaroniec, M. Gas adsorption characterization of ordered organic-inorganic nanocomposite materials. *Chem. Mater.* **2001**, *13*, 3169–3183. [CrossRef]
56. Limousin, G.; Gaudet, J.P.; Charlet, L.; Szenknect, S.; Barthès, V.; Krimissa, M. Sorption isotherms: A review on physical bases, modeling and measurement. *Appl. Geochem.* **2007**, *22*, 249–275. [CrossRef]

57. Carvalho, T.C.; La Cruz, T.E.; Tábora, J.E. A photochemical kinetic model for solid dosage forms. *Eur. J. Pharm. Biopharm.* **2017**, *120*, 63–72. [CrossRef] [PubMed]
58. Daugherty, J.P.; Hixon, S.C.; Yielding, K.L. Direct in vitro photoaffinity labeling of DNA with daunorubicin, adriamycin, and rubidazone. *BBA Sect. Nucleic Acids Protein Synth.* **1979**, *565*, 13–21. [CrossRef]
59. Hartman, P.E.; Biggley, W.H. Breakthrough of ultraviolet light from various brands of fluorescent lamps: Lethal effects on DNA repair-defective bacteria. *Environ. Mol. Mutagen.* **1996**, *27*, 306–313. [CrossRef]
60. Serpone, N. Relative photonic efficiencies and quantum yields in heterogeneous photocatalysis. *J. Photochem. Photobiol. A Chem.* **1997**, *104*, 1–12. [CrossRef]
61. Muff, J.; Bennedsen, L.R.; Søgaard, E.G. Study of electrochemical bleaching of p-nitrosodimethylaniline and its role as hydroxyl radical probe compound. *J. Appl. Electrochem.* **2011**, *41*, 599–607. [CrossRef]
62. Zhu, J.; Zheng, W.; He, B.; Zhang, J.; Anpo, M. Characterization of Fe-TiO_2 photocatalysts synthesized by hydrothermal method and their photocatalytic reactivity for photodegradation of XRG dye diluted in water. *J. Mol. Catal. A Chem.* **2004**, *216*, 35–43. [CrossRef]
63. Neubert, S.; Mitoraj, D.; Shevlin, S.A.; Pulisova, P.; Heimann, M.; Du, Y.; Goh, G.K.L.; Pacia, M.; Kruczała, K.; Turner, S.; et al. Highly efficient rutile TiO_2 photocatalysts with single Cu(II) and Fe(III) surface catalytic sites. *J. Mater. Chem. A* **2016**. [CrossRef]
64. Zhou, M.; Yu, J.; Cheng, B. Effects of Fe-doping on the photocatalytic activity of mesoporous TiO_2 powders prepared by an ultrasonic method. *J. Hazard. Mater.* **2006**, *137*, 1838–1847. [CrossRef]
65. Coleman, H.M.; Vimonses, V.; Leslie, G.; Amal, R. Removal of contaminants of concern in water using advance oxidation techniques. *Water Sci. Technol.* **2007**, *55*, 301–306. [CrossRef]
66. Coleman, H.M.; Abdullah, M.I.; Eggins, B.R.; Palmer, F.L. Photocatalytic degradation of 17[beta]-oestradiol, oestriol and 17[alfa]-ethynyloestradiol in water monitored using fluorescence spectroscopy. *Appl. Catal. B Environ.* **2005**, *55*, 23–30. [CrossRef]
67. Coleman, H.M.; Chiang, K.; Amal, R. Effects of Ag and Pt on photocatalytic degradation of endocrine disrupting chemicals in water. *Chem. Eng. J.* **2005**, *113*, 65–72. [CrossRef]
68. Lin, L.; Wang, H.; Jiang, W.; Mkaouar, A.R.; Xu, P. Comparison study on photocatalytic oxidation of pharmaceuticals by TiO_2-Fe and TiO_2-reduced graphene oxide nanocomposites immobilized on optical fibers. *J. Hazard. Mater.* **2017**, *333*, 162–168. [CrossRef] [PubMed]
69. Hamadanian, M.; Reisi-Vanani, A.; Behpour, M.; Esmaeily, A.S. Synthesis and characterization of Fe,S-codoped TiO_2 nanoparticles: Application in degradation of organic water pollutants. *Desalination* **2011**, *281*, 319–324. [CrossRef]
70. Naik, B.; Parida, K.M. Solar Light Active Photodegradation of Phenol over a $Fe_xTi_{1-x}O_{2-y}N_y$ Nanophotocatalyst. *Ind. Eng. Chem. Res.* **2010**, *49*, 8339–8346. [CrossRef]
71. Bloh, J.Z.; Dillert, R.; Bahnemann, D.W. Zinc Oxide Photocatalysis: Influence of Iron and Titanium Doping and Origin of the Optimal Doping Ratio. *ChemCatChem* **2013**, *5*, 774–778. [CrossRef]
72. Lorenz, R.D. A simple webcam spectrograph. *Am. J. Phys.* **2014**, *82*, 169–173. [CrossRef]
73. Widiatmoko, E.; Widayani; Budiman, M.; Abdullah, M.; Khairurrijal. A simple spectrophotometer using common materials and a digital camera. *Phys. Educ.* **2011**, *46*, 332–339. [CrossRef]
74. Altomare, A.; Corriero, N.; Cuocci, C.; Falcicchio, A.; Moliterni, A.; Rizzi, R. QUALX2.0: A qualitative phase analysis software using the freely available database POW_COD. *J. Appl. Crystallogr.* **2015**, *48*, 598–603. [CrossRef]
75. Spurr, R.A.; Myers, H. Quantitative Analysis of Anatase-Rutile Mixtures with an X-ray Diffractometer. *Anal. Chem.* **1957**, *29*, 760–762. [CrossRef]
76. Kim, C.; Park, H.J.; Cha, S.; Yoon, J. Facile detection of photogenerated reactive oxygen species in TiO_2 nanoparticles suspension using colorimetric probe-assisted spectrometric method. *Chemosphere* **2013**, *93*, 2011–2015. [CrossRef]
77. Simonsen, M.E.; Muff, J.; Bennedsen, L.R.; Kowalski, K.P.; Søgaard, E.G. Photocatalytic bleaching of p-nitrosodimethylaniline and a comparison to the performance of other AOP technologies. *J. Photochem. Photobiol. A Chem.* **2010**, *216*, 244–249. [CrossRef]
78. Kraljic, I.; Trumbore, C.N. p-Nitrosodimethylaniline as an OH radical scavenger in radiation chemistry. *J. Am. Chem. Soc.* **1965**, *87*, 2547–2550. [CrossRef]

79. Farhataziz, A.B.R. *Selected Specific Rates of Reactions of Transients from Water in Aqueous Solutions III: Hydroxyl Radical and Perhydroxyl Radical and Their Radical Ions*; U.S. Department of Commerce: Washington, DC, USA, 1977.
80. Martínez-Huitle, C.A.; Quiroz, M.A.; Comninellis, C.; Ferro, S.; De Battisti, A. Electrochemical incineration of chloranilic acid using Ti/IrO_2, Pb/PbO_2 and Si/BDD electrodes. *Electrochim. Acta* **2004**, *50*, 949–956. [CrossRef]
81. Bors, W.; Michel, C.; Saran, M. On the nature of biochemically generated hydroxyl radicals. Studies using the bleaching of p-nitrosodimethylaniline as a direct assay method. *Eur. J. Biochem.* **1979**, *95*, 621–627. [CrossRef] [PubMed]
82. Barashkov, N.N.; Eisenberg, D.; Eisenberg, S.; Shegebaeva, G.S.; Irgibaeva, I.S.; Barashkova, I.I. Electrochemical chlorine-free AC disinfection of water contaminated with Salmonella typhimurium bacteria. *Russ. J. Electrochem.* **2010**, *46*, 306–311. [CrossRef]
83. Hurwitz, A.R.; Liu, S.T. Determination of aqueous solubility and pKa values of estrogens. *J. Pharm. Sci.* **1977**, *66*, 624–627. [CrossRef]
84. Ying, G.G.; Kookana, R.S.; Ru, Y.J. Occurrence and fate of hormone steroids in the environment. *Environ. Int.* **2002**, *28*, 545–551. [CrossRef]
85. Fernández-Ibáñez, P.; De Las Nieves, F.J.; Malato, S. Titanium Dioxide/Electrolyte Solution Interface: Electron Transfer Phenomena. *J. Colloid Interface Sci.* **2000**, *227*, 510–516. [CrossRef]
86. George, S.; Pokhrel, S.; Ji, Z.; Henderson, B.L.; Xia, T.; Li, L.; Zink, J.I.; Nel, A.E.; Mädler, L. Role of Fe doping in tuning the band gap of TiO_2 for the photo-oxidation-induced cytotoxicity paradigm. *J. Am. Chem. Soc.* **2011**, *133*, 11270–11278. [CrossRef]
87. Bhatu, M.N.; Lavand, A.B.; Malghe, Y.S. Visible light photocatalytic degradation of malachite green using modified titania. *J. Mater. Res. Technol.* **2018**. [CrossRef]
88. Tabasideh, S.; Maleki, A.; Shahmoradi, B.; Ghahremani, E.; McKay, G. Sonophotocatalytic degradation of diazinon in aqueous solution using iron-doped TiO_2 nanoparticles. *Sep. Purif. Technol.* **2017**, *189*, 186–192. [CrossRef]
89. Aba-Guevara, C.G.; Medina-Ramírez, I.E.; Hernández-Ramírez, A.; Jáuregui-Rincón, J.; Lozano-Álvarez, J.A.; Rodríguez-López, J.L. Comparison of two synthesis methods on the preparation of Fe, N-Co-doped TiO_2 materials for degradation of pharmaceutical compounds under visible light. *Ceram. Int.* **2017**, *43*, 5068–5079. [CrossRef]
90. Hemmati Borji, S.; Nasseri, S.; Mahvi, A.; Nabizadeh, R.; Javadi, A. Investigation of photocatalytic degradation of phenol by Fe(III)-doped TiO_2 and TiO_2 nanoparticles. *J. Environ. Health Sci. Eng.* **2014**, *12*, 101. [CrossRef] [PubMed]